

# TIME-DISTANCE HELIOSEISMOLOGY WITH $f$ MODES AS A METHOD FOR MEASUREMENT OF NEAR-SURFACE FLOWS

T. L. DUVALL JR.<sup>1</sup> and L. GIZON<sup>2</sup>

<sup>1</sup>*Laboratory for Astronomy and Solar Physics, NASA/Goddard Space Flight Center, Greenbelt, MD 20771, U.S.A.*

<sup>2</sup>*W. W. Hansen Experimental Physics Laboratory, Stanford University, Stanford, CA 94305, U.S.A.*

(Received 18 October 1999; accepted 3 February 2000)

**Abstract.** Travel times measured for the  $f$  mode have been used to study flows near the solar surface in conjunction with simultaneous measurements of the magnetic field. Previous flow measurements of Doppler surface rotation, small magnetic feature rotation, supergranular pattern rotation, and surface meridional circulation have been confirmed. In addition, the flow in supergranules due to Coriolis forces has been measured. The spatial and temporal power spectra for a six-day observing sequence have been measured.

## 1. Introduction

The fundamental, or  $f$ , modes are classified as surface gravity waves with very nearly the classical water-wave dispersion relation,  $\omega^2 = gk$ , where  $\omega$  is the angular frequency,  $g = 274 \text{ m s}^{-2}$  is the gravitational acceleration at the Sun's surface, and  $k = (l + 1/2)/R_\odot$  is the horizontal spatial wavenumber expressed in terms of spherical harmonic degree  $l$  and solar radius  $R_\odot$ . On the Sun,  $f$  modes are excited with a similar frequency envelope to the acoustic  $p$  modes, peaking near circular frequency  $\nu = \omega/2\pi = 3 \text{ mHz}$  with a full width at half maximum of 1 mHz. The envelope peak occurs near  $l = 880$  and the full power width covers the degree range 600–1200. In this range the  $f$ -mode kinetic energy is concentrated within 2 Mm of the solar photosphere.

There are several advantages to using the  $f$  mode as a tracer of flows near the solar surface. Using the time-distance technique, there is direct sensitivity to both horizontal components of the flow. Already this is much better than direct Doppler measurements, which see only the line-of-sight component. In this respect the  $f$ -mode time-distance technique is similar to correlation tracking of granulation and in fact has been compared directly with that technique (DeRosa, Duvall, and Toomre, 2000). Other techniques for measuring vector flows include ring diagrams (Hill, 1988),  $p$ -mode time-distance helioseismology (Duvall *et al.*, 1996) and knife-edge diagnostics (Lindsey *et al.*, 1996). With  $f$  modes, there is no direct sensitivity to vertical motion, although by examining the horizontal divergence it would be possible to estimate the vertical motion. Because we know the  $f$ -mode eigenfunctions, the depth over which we are averaging is well defined.



As  $f$  modes have not been used in this way before, the purpose of this work is to test the usefulness of the technique by first observing well-known phenomena, and then extend to harder problems. To this end, we simultaneously measure three tracers of solar rotation that in the past have given similar, yet consistently different rotation rates (Beck and Schon, 2000). By using the same instrument with simultaneous observations, we expect that some of the possible systematic errors will be common. The tracer that gives the highest apparent rotation rates is the supergranulation patterns (Duvall, 1980; Snodgrass and Ulrich, 1990). The second tracer we use is the small magnetic features determined from cross correlation (Komm, Howard, and Harvey, 1993). The third tracer we use is the  $f$ -mode advection, which we identify as a proxy of the surface rotation, as it is an average over 2 Mm near the surface. This is compared to the surface Doppler rate averaged over 18 years by Snodgrass and Ulrich (1990).

An interesting effect that can be studied with both horizontal components of the supergranular velocity is that of the Coriolis force. This was studied theoretically for a simplified solar convection model by Hathaway (1982). Cellular convection in a rotating incompressible fluid was also studied by Veronis (1959). In these models, the Coriolis force causes divergent and convergent horizontal flows to be associated with vertical components of vorticity of opposite signs. In the northern hemisphere, the cell rotates clockwise where the horizontal divergence is positive, while it rotates counterclockwise in the convergent flow towards the sinks. A corresponding pattern of streamlines is shown in Figure 1. The sense of circulation is reversed in the southern hemisphere and the amplitude is proportional to the radial component of rotation. The cell rotation in the divergent flow was apparently detected by Kubičela (1973), which is quite remarkable considering the primitive state of technology at that time.

## 2. Observations and Analysis

### 2.1. PROCEDURE

MDI full-disk Dopplergrams and magnetograms (Scherrer *et al.*, 1995) were used to study flows for the time period 14 April 1999, 16 h UT to 20 April 1999, 16 h UT, or a total of six days. The region studied was nominally centered at Carrington longitude  $180^\circ$ . This particular region was picked because it was quiet and the data coverage was very good as it was during MDIs three months of continuous coverage for 1999 (97.3% of the minutes had usable data during the six days). Three separate regions were studied, with all three of size  $45^\circ$  in longitude and in latitude, with one centered on the equator, one centered at  $40^\circ$  north and the other at  $40^\circ$  south. There is some overlap between the regions, and as the equatorial and higher latitude areas were tracked at different rotation rates, this difference was used to calibrate one of the signals, as described below. The  $B_0$  angle was  $-5^\circ$

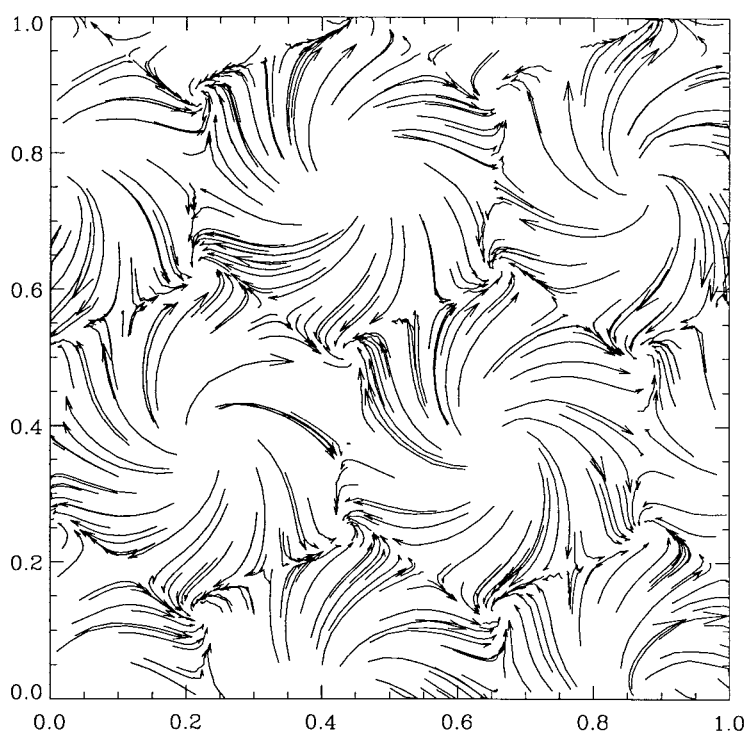


Figure 1. A sketch of horizontal streamlines in rotating hexagonal convection cells (Veronis, 1959). The rotation vector is coming out of the page.

during the observations, and we estimate that latitudes ranging from  $-55^\circ$  to  $+45^\circ$  can be analyzed safely.

Doppler images were calibrated and located in the CCD frame using the normal MDI pipeline routines. The first step in the analysis is the tracking of the regions to be studied. Images were interpolated onto Postel's azimuthal equidistant projection (Pearson, 1990) centered on a point in latitude  $0^\circ$ ,  $+40^\circ$ ,  $-40^\circ$  and at longitude  $180^\circ$ . The azimuthal equidistant projection is linear in great-circle distance measured from the central point of the projection to outlying points. This projection is used rather than a longitude-sin(latitude) projection so that three-dimensional Fourier filtering can be used on the data more effectively. The regions were followed at a rate appropriate for the central latitude and consistent with the supergranule pattern rate measured by Snodgrass and Ulrich (1990). During the time period of the observations MDI was observing both full-disk Dopplergrams and magnetograms with one-minute cadence. Both Dopplergrams and magnetograms were processed by the above procedure so that detailed comparisons between the two could be made. A smooth background image (spatial scale  $0.2 R_\odot$ ) was subtracted from each Dopplergram before the projection.

The magnetograms were also processed to remove cosmic rays and smoothed in time. To remove the effect of cosmic rays striking the CCD during the exposure/readout, the temporal pixel-by-pixel median of three successive images was taken and the resultant median replaced the middle image. The cosmic rays commonly affect pixels in a small neighborhood but only for a single image and so are generally removed by the median procedure. This procedure also smooths the field on a three-minute time scale. After the median procedure, images over a ten-minute interval are averaged and a new time series is constructed of these ten-minute means.

To obtain travel times, a similar procedure is used as for  $p$  modes (Duvall *et al.*, 1997), except that the filtering is a little different. For each 8-hrs interval, the datacube goes through a three-dimensional Fourier filter that (1) cuts off power below 2 mHz (mostly supergranulation), (2) isolates the  $f$  mode, and (3) filters the spectrum for a range of horizontal phase speeds. In the present case, after the filtering, a spectrum is computed. The resultant spectrum peaks near  $\nu = 2.9$  mHz and spherical harmonic degree  $l = 800$ . The full widths at half maximum are  $\Delta\nu = 0.7$  mHz and  $\Delta l = 400$ . Figure 2 displays the corresponding average kinetic energy density versus depth. We see that we can probe the first 2 Mm below the solar surface for this distribution of degrees.

The temporal signal at a spatial pixel is cross-correlated with the signals in the four quadrants of an annulus centered in arc distance on the spatial pixel. These quadrants are centered on the cardinal directions north, south, east, and west. For each cross-correlation, the information for waves propagating from the center to the quadrant is separated from that for waves propagating from the quadrant to the center, with one showing up at positive shifts of the correlation and the other at negative shifts. Before measuring the travel times, average cross-correlations are made for the waves propagating in the cardinal directions and additional averages are made for waves propagating outwards from the center and inwards toward the center. The difference between outward and inward times is proportional to the horizontal divergence of the flow. And one final mean is made that averages all the cross-correlations for that pixel. In addition, to make the signal-to-noise acceptable, the cross-correlations for a  $2 \times 2$  grid of origins are averaged, thereby reducing the spatial resolution of the resultant maps by a factor of two below that of the original data.

The thickness of an individual annulus is the same as the spatial sampling of the original images, or  $0.12^\circ$ . Four of these are combined during the fitting process, and so all pixels from  $0.42^\circ$  to  $0.90^\circ$  are used in the measurements. The angle  $0.9^\circ$  corresponds to a distance of 7.5 pixels in the original spatial sampling and 3.75 in the reduced spatial scale.

The cross-correlations were then fit by least squares to a harmonic function multiplied by a gaussian envelope, sometimes called a Gabor wavelet. This form has been developed for the case of  $p$  modes (Kosovichev and Duvall, 1997), but seems to work reasonably well for the  $f$  modes also. An analysis optimized for

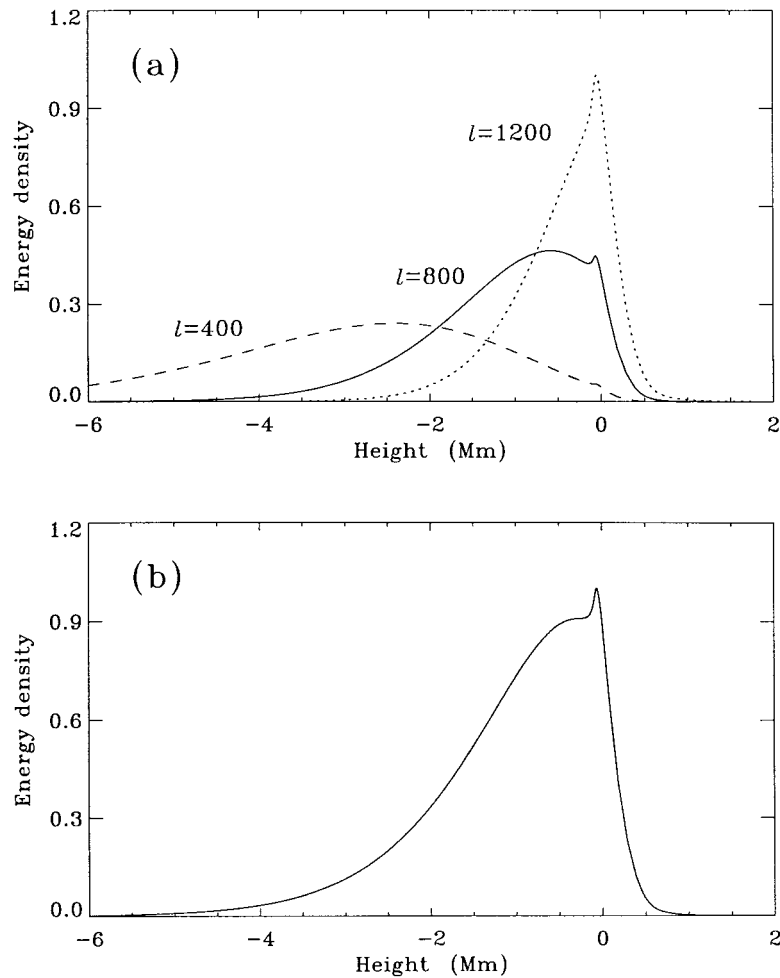


Figure 2. (a) Kinetic energy density versus height for  $f$  modes with degrees 400, 800, and 1200. Calculations are for a plane-parallel atmosphere with constant gravity. The height is measured from the photosphere (radius 695.99 Mm). A free surface is placed 2 Mm above the photosphere. The internal density is taken from the standard solar model of Christensen-Dalsgaard, Proffitt, and Thompson (1993). Above the temperature minimum, density is from the chromospheric model C of Vernazza, Avrett, and Loeser (1981). Curves are normalized to the same arbitrary constant. (b) Average kinetic energy density versus height for the  $f$  modes used in this study. The mean and standard deviation of this distribution are, respectively,  $-1.05$  Mm and  $1.01$  Mm. The location of the absolute maximum coincides with the highly superadiabatic layer.

$f$  modes is under development. The travel time used is from the phase of the harmonic function divided by the frequency, the so-called phase time. The difference between phase times for counter-propagating waves should be proportional to the local flow velocity (Kosovichev and Duvall, 1997).

## 2.2. SUPERGRANULATION

An example of the divergence signal (inward minus outward travel time) for one of the 18 8-hrs intervals analyzed is shown in Figure 3 with magnetic field information overlaid. A white, or positive signal, corresponds to an outflow from the center. From the size of the features present, their lifetime, and the presence of the magnetic field in the dark lanes, we identify supergranulation as the main contributor to the signal. This can also be seen by making a power spectrum of the 18 frames covering the 6 days. Averaging over all temporal frequencies, the resultant spatial spectrum is shown in Figure 4. The peak near degree  $l = 120$  is characteristic of the supergranulation and has been seen before in the surface Doppler observations (e.g., Hathaway *et al.*, 2000). The peak in the zero-frequency bin is due to the nonzero mean of the divergence signal ( $-0.16 \pm 0.02$  s), for which we have no explanation. The histogram of the divergence signal is shown in Figure 5. An asymmetry between the regions of divergent and convergent flows is clearly seen. There are more points associated with a convergent flow than with a divergent one, and the distribution is skewed. It should be noted that both these properties are present in Veronis' model for hexagonal cells; although they are not in the case of square cells.

As far as we know, the present study is the longest time that supergranules have been studied by a method that measures both horizontal components of velocity. For this reason it is useful to examine the temporal spectrum to study its low frequency behavior. In Figure 6 we show the temporal power spectrum of the divergence signal averaged over all spatial frequencies. We see that much of the power is at very low frequencies, with 85% of the power below  $6 \mu\text{Hz}$ . This is reasonably consistent with a Lorentzian-shaped temporal spectrum, as suggested in the Harvey (1985) model. We also studied the temporal correlation of these images and found that it was significantly negative ( $-0.1$ ) at a time lag of 3 days, consistent with the results of Shine, Simon, and Hurlburt (2000) that new supergranules appear near the boundaries of old supergranules.

## 2.3. DIFFERENTIAL ROTATION AND CORIOLIS FORCE

To study rotation of the supergranulation velocity pattern, one-dimensional spatial cross-correlations were computed for our  $f$ -mode divergence signal for times separated by eight hours for all lines separately. The cross-correlations for the different pairs are averaged and then fit to a gaussian function. The spatial shift is converted to a longitude, divided by 8 hrs, and added to the tracking rate to determine a rotation rate. The procedure for the small magnetic features is similar except that the time difference is 10 min as this gave the smallest errors.

To measure the  $f$ -mode advection rotation rate, the east-west travel-time difference is averaged in  $5^\circ$  latitude bins. The signal is calibrated by using the different tracking rates for the north and south regions. By requiring that the rotation rate in the overlap region be the same for the equatorial tracked data and for the northern

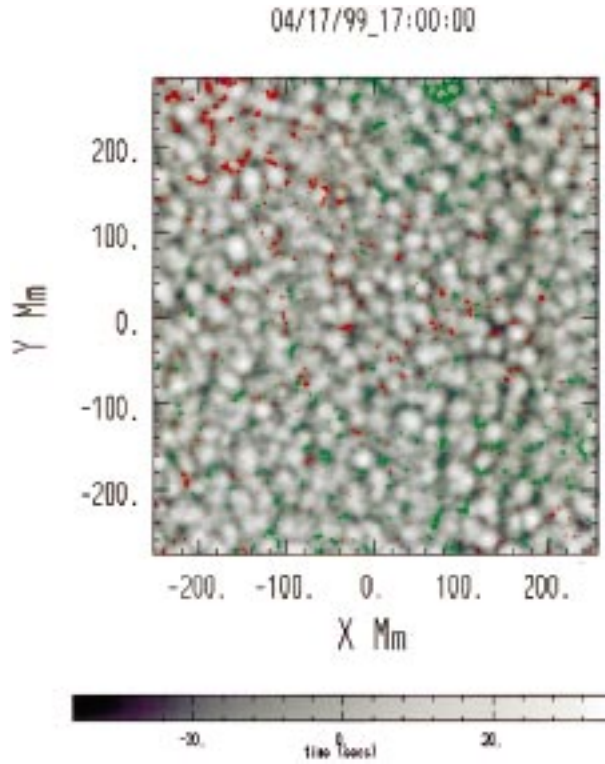


Figure 3. Example of the divergence signal (inward travel times minus outward times) with magnetic field signal overlaid. Magnetic field is displayed as green and red for the two polarities when the magnitude of the field is larger than 15 G. The gray scale is for the divergence signal with white shades for outflow and dark shades for inflow. The color bar indicates the travel-time difference in seconds. The line  $Y = 0$  corresponds to the equator and  $X = 0$  corresponds to Carrington longitude  $180^\circ$ . The time-distance data is averaged over 8.5 hrs starting at the time shown on top.

tracked data, we derive a unique calibration constant. As a check, we then compare the rotation rate in the overlap region between the equatorial and southern tracked region and find agreement within 0.3 nHz. The calibration constant  $\alpha$  which relates the westward flow to the travel-time difference (eastward minus westward) is found to be  $\alpha = 7.08 \text{ m s}^{-2}$ .

On the other hand, at fixed frequency, the ray approximation can be used to estimate the wavenumber perturbation caused by the flow, which then yields  $\alpha \sim 1.11 g / (4 l_0 \Delta)$ , where  $l_0$  is the central spherical harmonic degree of the wavepacket and  $\Delta$  is the mean angular distance between the central point and the quadrants. The factor 1.11 is due to the quadrant geometry. For  $l_0 = 870$  and  $\Delta = 0.66^\circ$ , ray theory gives  $\alpha \sim 7.60 \text{ m s}^{-2}$ , or 7% higher than our calibration constant. There are several reasons why we do not use this ‘theoretical’ calibration, including that  $l_0$  and  $\Delta$  are not so easy to estimate.

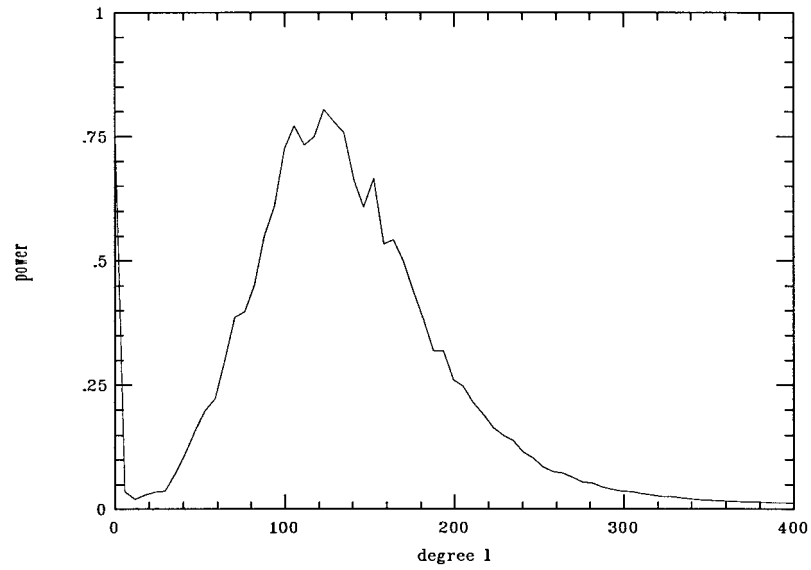


Figure 4. Power versus horizontal wavenumber averaged over temporal frequency and azimuth for the divergence signal (inward travel times minus outward times). The power scale is arbitrary.

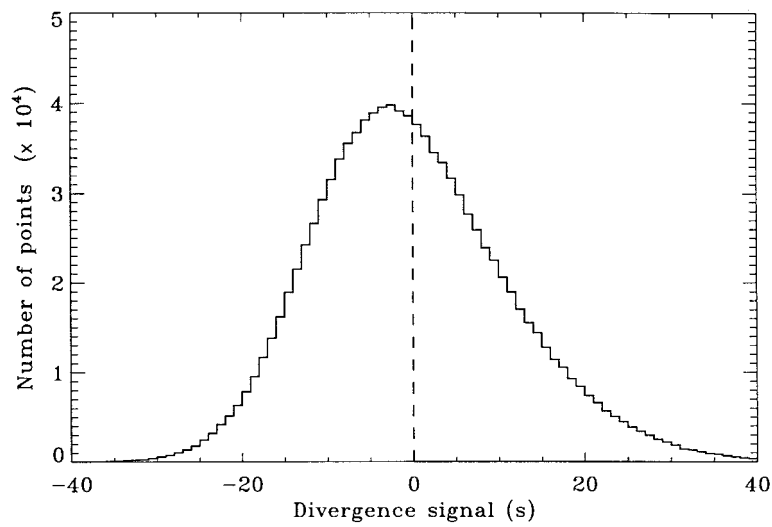


Figure 5. Histogram of the divergence signal (inward travel times minus outward times). The maximum of the histogram occurs near  $-2.5$  s and the skewness is 0.42. There are about 20% more points with negative divergence than positive divergence.

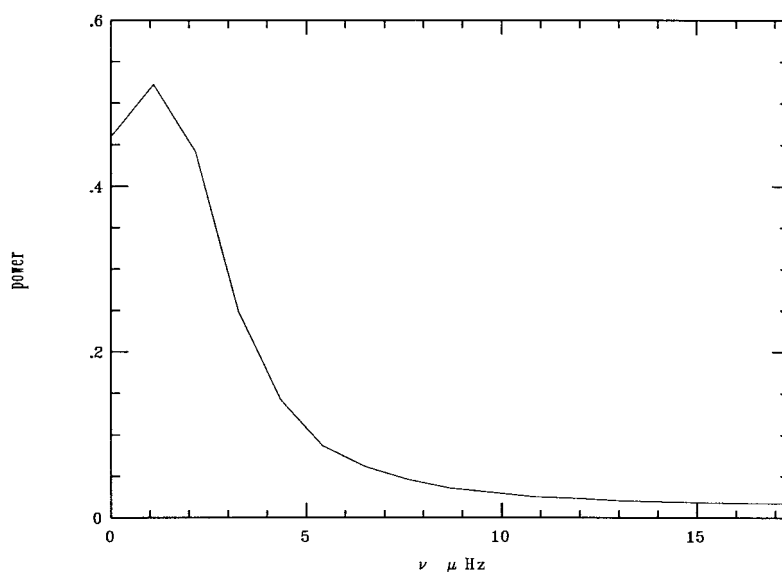


Figure 6. Power versus temporal frequency averaged over horizontal wavenumber for the divergence signal (inward travel times minus outward times). The power scale is arbitrary.

The  $f$ -mode advection rotation rate is compared with the long-term average of the surface Doppler rate in Figure 7(a). We see that the two agree rather well. We have also measured the near-surface meridional circulation from the south-north travel times using the calibration derived for the rotation. The results are shown in Figure 7(b), compared with the magnetic features measured by Meunier (1999). It appears that from six days of data we can also make remarkably consistent measurements of meridional circulation.

The three rotation measures are compared with previous work in Figure 8. We find that there is good agreement with the earlier work averaged over decades. This figure supports the small but consistent rotation differences between these variables. It was suggested long ago (Foukal, 1972) that the difference between the rotation of magnetic patterns and the surface Doppler rate may be due to magnetic structures being 'rooted' in deeper, more rapidly rotating layers. The relatively high supergranulation rate is more puzzling. Hathaway (1982) suggested that a faster supergranular rate may be a direct consequence of the interaction of convection and rotation.

To learn more about the small difference between the supergranular rate and the small magnetic feature rate, we examined a movie made from frames similar to Figure 3. The largest effect seen in the movie was the residual differential rotation with latitude, which was very distracting. This effect was removed by using the supergranular feature rate from Snodgrass and Ulrich (1990) to suppress the differential rotation from both the divergence images and from the magnetic images. The resultant movie had features that were motionless except for evolution. A small

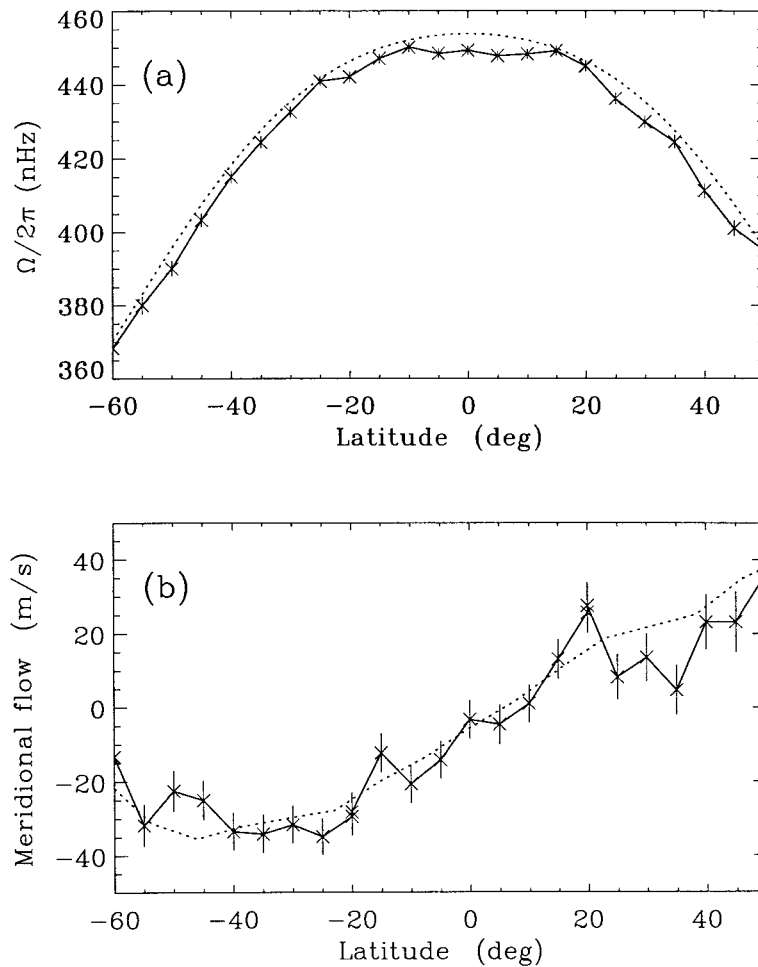


Figure 7. (a)  $f$ -mode advection rotation rate (solid curve) and surface Doppler rotation (dashed curve) versus latitude. The  $f$ -mode rate corresponds to  $\sim 1$  Mm below the surface. The surface Doppler rate is the average from 1967–1984 given by Snodgrass and Ulrich (1990), which is found to be 3.4 nHz higher on average. (b) Meridional circulation versus latitude. The solid curve and crosses are the  $f$ -mode measurements. The dashed curve is from the magnetic measurements of Meunier (1999) for the first year of MDI operation in 1996–1997.

motion of the magnetic features in the eastward direction (slower rotation) was also visible. The magnetic features stayed in the dark lanes as this slow apparent drift took place. Note that with the rotation frequency difference of 10 nHz the magnetic features should move about a supergranular diameter during the six days of observations.

To study how the Coriolis force affects the supergranular flow, we computed local values of the radial component of the curl of the velocity field using the east–west signal and south–north signal as the two horizontal components of velocity.

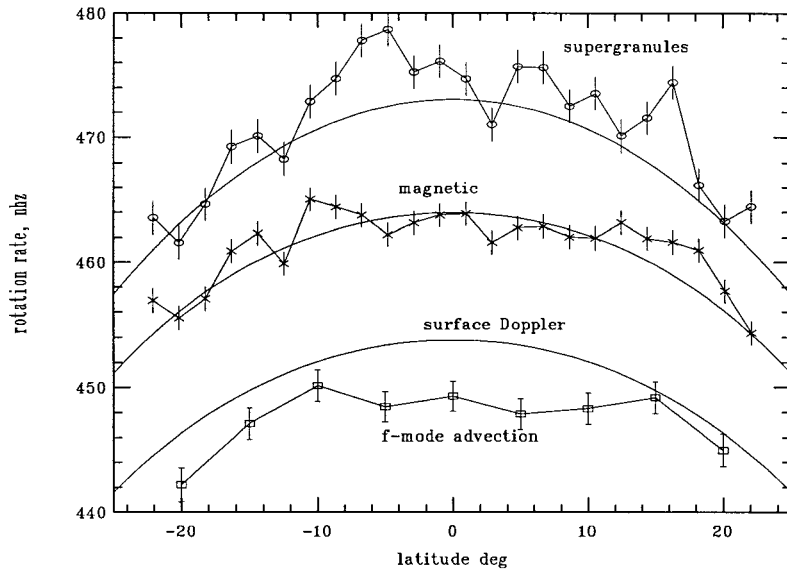


Figure 8. Rotation rates measured in this work compared with previous work. From the top, the open circles with error bars are derived from the supergranular patterns of the divergence signal (this work) and the solid line through the values is the supergranular feature rate averaged for years 1967–1987 by Snodgrass and Ulrich (1990). In the middle, the crosses with error bars are from the MDI magnetic correlations (this work) and the underlying solid line plots the average over years 1975–1991 of the small magnetic feature rate (Komm, Howard, and Harvey, 1993). At the bottom, the open squares with error bars are the  $f$ -mode advection measurements from this study and the nearby solid line is from the average surface Doppler rotation rate (1967–1984) of Snodgrass and Ulrich (1990).

This value of the curl is divided by the local absolute magnitude of the horizontal divergence of the flow. The derivatives are approximated using the standard second order centered difference. Division by the divergence is a reasonable way to normalize the curl as suggested by Veronis' model (see Appendix). Averages of  $\text{curl}/|\text{div}|$  are made in regions of positive and negative divergence separately. When the divergence has a small magnitude, the point is however not used (about 15% of the points). The plot of these versus latitude is shown in Figure 9. We see that the sense of circulation matches that outlined in the introduction and hence attribute this signal to the effect of the Coriolis force on the supergranulation. Although differential rotation and meridional circulation may contribute to the vorticity and divergence, they would not introduce a component of  $\text{curl}/|\text{div}|$  with the functional form (or magnitude) depicted in Figure 9. To get the overall average effect, we divide the curl by the divergence (as opposed to its absolute value). Averages of this quantity are displayed in Figure 10 as a function of latitude  $\lambda$ , along with a curve with the  $\Omega(\lambda) \sin \lambda$  dependence we might expect (see Appendix).

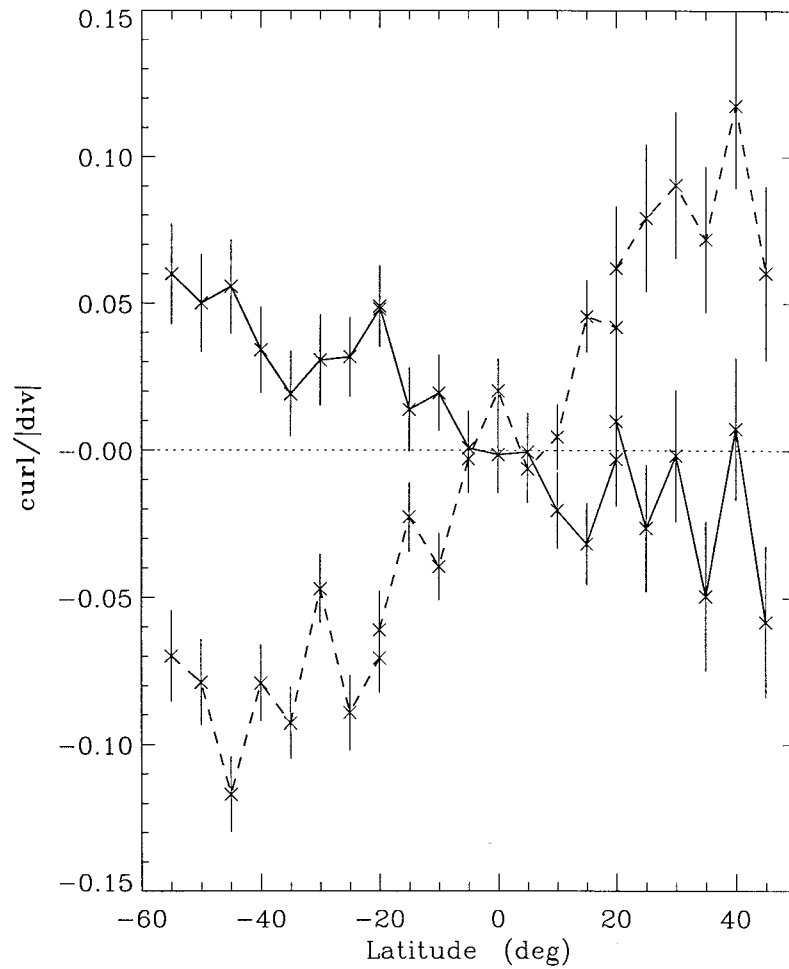


Figure 9. Plot of  $\text{curl}/|\text{div}|$  for divergent flow regions (*solid curve*) and for convergent flow regions (*dashed curve*). The change in sign of both curves at the equator and the opposite sign of the two curves both are indicators that what we are seeing is the effect of the Coriolis force on the supergranular flow.

### 3. Conclusions

Time-distance helioseismology of the  $f$  mode has been shown to be a useful tool to study horizontal flows near the solar surface. In addition, we have found simultaneous measurements of velocity and magnetic field with MDI to be a powerful combination to study dynamics near the solar surface.

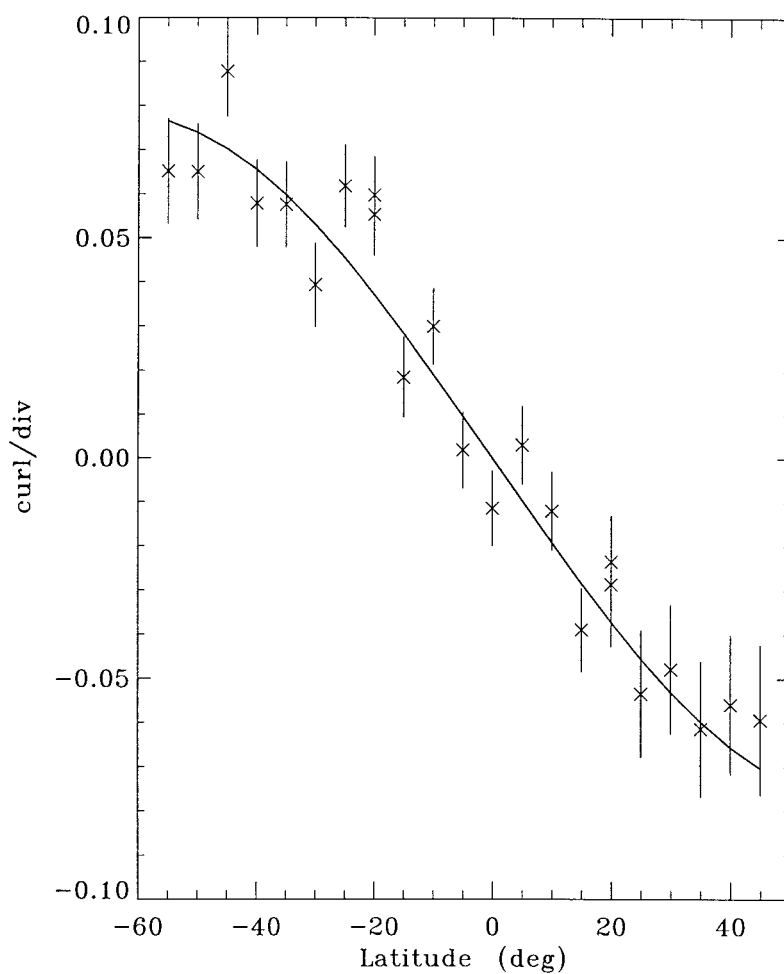


Figure 10. The radial component of the curl divided by the horizontal divergence (crosses) as a function of latitude  $\lambda$ . The solid curve is a fit of the  $\Omega(\lambda) \sin \lambda$  dependence, where  $\Omega(\lambda)$  is the angular velocity of Snodgrass and Ulrich (1990).

### Appendix

The problem of steady cellular convection in a rotating incompressible fluid was investigated by Veronis (1959). Given a horizontal layer of fluid confined between two free boundaries and subject to a vertical temperature gradient, he obtained explicit modal solutions. These solutions are expressed in terms of the dimensionless Taylor number  $T = 4\Omega_z^2 d^4 / \bar{\nu}^2$ , where  $d$  is the thickness of the layer,  $\bar{\nu}$  is the kinematic viscosity of the fluid, and  $\Omega_z$  is the angular velocity about the vertical axis  $\hat{\mathbf{z}}$ . For the lowest-order convection mode, and when cells are either square or hexagonal, the horizontal velocity  $\mathbf{U}_\perp$  satisfies the following property everywhere:

$$C \equiv \frac{(\nabla_{\perp} \wedge \mathbf{U}_{\perp}) \cdot \hat{\mathbf{z}}}{\nabla_{\perp} \cdot \mathbf{U}_{\perp}} = -\frac{T^{1/2}}{\pi^2[1 + (2d/L)^2]}, \quad (1)$$

where  $L$  is the horizontal spatial periodicity of convection. A measure of  $C$  would provide a relationship between  $L$ ,  $d$  and  $\bar{\nu}$ .

This model is not intended to approximate well the Sun in that it has constant density and laminar flow (see, e.g., Simon and Weiss, 1968). However, it is useful since it is analytic and has many of the large-scale parameters of the problem present. Thinking in terms of orders of magnitude, it is of interest to see how the above formula applies to the supergranulation. A local area on the Sun may be approximated by a plane-parallel layer of fluid tangent to the sphere. At latitude  $\lambda$ , the effective angular velocity is given by the radial component of the local angular velocity vector  $\Omega(\lambda)$ . Thus, we have

$$C(\lambda) = \beta \Omega(\lambda) \sin \lambda, \quad (2)$$

where

$$\beta = -\frac{2d^2}{\bar{\nu} \pi^2[1 + (2d/L)^2]}. \quad (3)$$

Taking  $\Omega(\lambda)$  as measured by Snodgrass and Ulrich (1990), the fit shown in Figure 10 gives  $\beta = -3.9 \times 10^4$  s. Given a horizontal size  $L = 25$  Mm and a cell depth  $d = 8$  Mm (Duvall, 1998), we obtain  $\bar{\nu} \sim 250 \text{ km}^2 \text{ s}^{-1}$ . Surprisingly, this estimate of the (turbulent) viscosity is in agreement with the values published by Simon and Weiss (1997).

### Acknowledgements

This work was partially supported by NASA grant NAG5-3077 to Stanford University. We would like to thank John Beck for useful discussions. TLD would like to thank Phil Scherrer and the MDI group for their hospitality during this study.

### References

- Beck, J. G. and Schon, J.: 2000, *Solar Phys.* **192**, in press.  
 Christensen-Dalsgaard, J., Proffitt, C. R., and Thompson, M. J.: 1993, *Astrophys. J.* **403**, L75.  
 DeRosa, M., Duvall, T. L. Jr., and Toomre, J.: 2000, *Solar Phys.* **192**, 351 (this issue).  
 Duvall, T. L. Jr.: 1980, *Solar Phys.* **66**, 213.  
 Duvall, T. L. Jr.: 1998, *Structure and Dynamics of the Interior of the Sun and Sun-like Stars*, ESA SP-418, p. 581.  
 Duvall, T. L. Jr., D'Silva, S., Jefferies, S. M., Harvey, J. W., and Schou, J.: 1996, *Nature* **379**, 235.  
 Duvall, T. L. Jr., Kosovichev, A. G., Scherrer, P. H., Tarbell, T. D., Title, A. M., and Milford, P. N.: 1997, *Solar Phys.* **170**, 63.  
 Foukal, P.: 1972, *Astrophys. J.* **173**, 439.

- Harvey, J.: 1985, in Rolfe E. and Battrock B. (eds.), *Future Missions in Solar, Heliospheric, and Space Plasma Physics*, ESA SP-233, p. 199.
- Hathaway, D. H.: 1982, *Solar Phys.* **77**, 341.
- Hathaway, D. H. *et al.*: 2000, *Solar Phys.* **192**, in press.
- Hill, F.: 1988, *Astrophys. J.* **333**, 996.
- Komm, R. W., Howard, R. F., and Harvey, J. W.: 1993, *Solar Phys.* **145**, 1.
- Kosovichev, A. G. and Duvall, T. L. Jr.: 1997, in F. Pijpers *et al.* (eds.), *SCORE '96: Solar Convection and Oscillations and their Relationship*, Kluwer Academic Publishers, Dordrecht, Holland, p. 241.
- Kubičela, A.: 1973, in J. Xanthakis (ed.), *Solar Activity and Related Interplanetary and Terrestrial Phenomena*, Proceedings of the First European Astronomical Meeting, Springer-Verlag, Berlin, p. 123.
- Lindsey, C., Braun, D. C., Jefferies, S. M., Woodard, M. F., Fan, Y., Gu, Y., and Redfield, S.: 1996, *Astrophys. J.* **470**, 636.
- Meunier, N.: 1999, *Astrophys. J.* **527**, 967.
- Pearson, F.: 1990, *Map Projections: Theory and Applications*, CRC Press, Boca Raton.
- Scherrer, P. H., Bogart, R. S., Bush, R. I., Hoeksema, J. T., Kosovichev, A. G., Schou, J., Rosenberg, W., Springer, L., Tarbell, T. D., Title, A., Wolfson, C. J., Zayer, I. and the MDI Engineering Team: 1995, *Solar Phys.* **162**, 129.
- Shine, R. A., Simon, G. W., and Hurlburt, N. E.: 2000, *Solar Phys.* **192**, in press.
- Simon, G. W. and Weiss, N. O.: 1968, *Z. Astrophys.* **69**, 435.
- Simon, G. W. and Weiss, N. O.: 1997, *Astrophys. J.* **489**, 960.
- Snodgrass, H. B. and Ulrich, R. K.: 1990, *Astrophys. J.* **351**, 309.
- Vernazza, J. E., Avrett, E. H., and Loeser, R.: 1981, *Astrophys. J. Suppl.* **45**, 635.
- Veronis, G.: 1959, *J. Fluid Mech.* **5**, 401.